Journal of Materials Chemistry A

Accepted Manuscript

ROYAL SOCIETY OF CHEMISTRY

www.rsc.org/materialsA

Journal Name

ARTICLE

Fabrication and Structural Optimization of Porous Single-crystal α-Fe_2O_3 Microrices for High-Performance Lithium-ion Battery Anode†

Received 00th January 20xx,
Accepted 00th January 20xx

DOI: 10.1039/x0xx00000x

www.rsc.org/

Bao Zhi Yu,‡[a] Xiao Li Liu,‡[b] Hui Gang Zhang,[c] Guang Yin Jing,[d] Pei Ma,[b] Yane Luo,[b] Wei Ming Xue,[b] Zhao Yu Ren*[a] and Hai Ming Fan*[ab]

Three-dimensional (3D) porous frameworks have great promise on the field of lithium-ion batteries (LIB). However, the size effects which 3D porous frameworks have on the structural and functional optimization are rarely reported. Herein, porous single-crystal α-Fe_2O_3 microrices synthesized through a facile one-pot hydrothermal method have been developed as a model system to investigate the correlations between pore structure and LIB performance. A top-down chemical etching method was used to control the pore size and porosity of the α-Fe_2O_3 microrices simultaneously over a wide range. The α-Fe_2O_3 porous microrices were further coated with carbon to stabilize the structure. The electrochemical characterizations show that the increase of the pore size and the total porosity leads to a higher specific capacity but poorer cycling performance. Carbon coating on the surface of α-Fe_2O_3 microrices significantly enhance the structural stability of particles and improve the cyclability of batteries. The obtained α-Fe_2O_3@C porous microrices exhibit a high capacity of ~1107 mAh g^{-1} at a current density of 200 mA g^{-1}, 83% capacity retention after 100 cycles and an excellent rate capability, which are among the best ones so far reported for α-Fe_2O_3 electrodes. Our results provide a general structural optimization strategy of porous oxides for high performance LIB anodes.

Introduction

Lithium-ion batteries (LIBs) as one of the most important energy storage systems are widely used because of their high energy density and environmental friendliness.[1-7] However, the lifetime and power density of current LIBs can not satisfy the ever increasing requirements.[8-12] It is known that the performance of LIB electrodes is generally determined by the thermodynamic and kinetic behaviour of the Li^+ ions, which is strongly influenced by the intrinsic physical-chemical properties and morphology of electrodes materials.[13,14] Transition metal oxides (TMO) have stimulated tremendous scientific and technological interest due to their unique properties and applicability as the electrode materials.[15,16] Especially, hematite materials have attract increasing attention owing to its relative high theoretical capacity (1007 mAh g^{-1}), environmental friendliness, low cost and high resistance to corrosion.[17-24] However, the relatively poor ion or electron transport properties, large volume change and unstable solid electrolyte interphase (SEI) have been limiting the application of α-Fe_2O_3 anodes in LIBs.[25-27]

Considerable efforts have been made in the structural design for α-Fe_2O_3 electrode materials such as nanospheres,[17,18] nanoflakes,[19] nanotubes,[20] nanofiber,[21] hollow sphere[22,23] and so on, which have demonstrated that the nanostructured α-Fe_2O_3 can greatly improve their electrochemical performance. However, a significant amount of polymer binder is required to keep Fe_2O_3 nanoparticles in contact and adhere to current collectors, leading to a high resistance of the electrodes.[28] Moreover, low tap-density of nanoparticles reduces the practical energy density of batteries.[29] Compared to nanoscale particles, micro-sized α-Fe_2O_3 having high tap-density are easy to handle during electrode manufacturing.[30-33] Particularly, α-Fe_2O_3 micro-particles with three-dimensional (3D) porous structures have shown great potential in LIB application.[33] For example, single-crystal α-Fe_2O_3 melon-like porous micro-particles prepared by a selective oxalic acid etching process demonstrated that the porous microstructure manifest a significantly improved cycling stability for lithium storage.[33] Meanwhile, such single-crystal porous microstructures system constructed via the top-down strategy present better structural stability than that of micro-sized agglomerates composed of nano-sized primary crystallites. Ye *et al.*[13] argue that the pore size and total

[a] National Photoelectric Technology, Functional Materials and Application of Science and Technology International Cooperation Center, and Institute of Photonics and Photon-Technology, Northwest University, Xi`an, 710069, China. Email: rzy@nwu.edu.cn; fanhm@nwu.edu.cn
[b] School of Chemical Engineering, Northwest University, Xi'an, 710069, China.
[c] Department of Energy Science and Engineering, College of Engineering and Applied Sciences, Nanjing University, China.
[d] Department of Physics, Northwest University, Xi'an 710069, P. R. China.

† Electronic Supplementary Information (ESI) available: Particle size distribution statistics, XRD analysis of the products with a reaction time, N_2 adsorption-desorption isotherms and the SEM images of active materials after 100 cycles. See DOI: 10.1039/x0xx00000x

‡These authors contributed equally to the work.

porosity of porous materials play important roles in their LIB performance. By matching the Li^+ transportation in the liquid electrolyte and the solid-state active material phases through adjusting pore size and thickness of the active coating, the significant improvements can be achieved for the performance of electrode materials. Although modest strides have been achieved, the structural optimization strategy for porous micro-sized single-crystal metal oxide is still not clear and urgently demanded.[13]

Here we demonstrate a model system of single-crystal α-Fe_2O_3 porous microrices prepared by a low-cost and effective one-step hydrothermal method. The porous framework is constructed via a top-down chemical etching approach. Tuning pore size and porosity by the reaction parameters enables systematically investigation of structural optimization of α-Fe_2O_3 porous microrices for LIBs application. Particularly, the pore size and porosity of microrices are found to increase simultaneously during the etching process. The electrochemical properties of as-synthesized porous α-Fe_2O_3 with different pore size have been conducted to reveal the correlations between the pore size/total pore volume and the capacity/cycling life. Furthermore, in order to compensate the possible loss of stability due to porous structure and enhance their conductivity[34,35], the effect of carbon coating on LIB performance of porous α-Fe_2O_3 microrices has also been investigated. This study aims to provide a structural optimization strategy to generate comprehensive high performance porous micro-scale oxides electrode materials, which is instructive to promoting the developments of micro-scale materials in LIB applications.

Experimental

Materials Synthesis

In a typical synthesis of the Fe_2O_3 porous microrices, 6.4 mL of aqueous $FeCl_3$ solution (0.5 M) and 0.72 mL of aqueous $NH_4H_2PO_4$ solution (0.02 M) were mixed. Distilled water was added to a final volume of 40 mL. After stirring for 10 minutes, the mixture was transferred into a Teflon-lined stainless-steel autoclave with a capacity of 50 mL for hydrothermal treatment at 220 °C. A series of experiments were carried out at different hydrothermal reaction times to investigate the structural evolution process. The autoclave was naturally cooled down to room temperature. The precipitate was separated by centrifugation, washed with distilled water and absolute ethanol, and then dried under vacuum at 80 °C.

For carbon coating process, 0.5 g porous Fe_2O_3 microrices were added to a transparent solution containing 0.5 g citric. For carbon coating process, 0.5 g porous Fe_2O_3 microrices were added to a transparent solution containing 0.5 g citric acid and 5 mL ethanol and stirred in a sealed bottle for 24 h.[34] After filtrating and drying, the final powder was sintered at 300 °C for 2 h in Ar gas.

Fig. 1 A schematic illustration of the synthetic procedure of porous α-Fe_2O_3 @C microrices.

Characterization

X-ray diffraction (XRD) was conducted within a D8 Advance X-ray diffractometer. The morphologies of the powder were studied by Field emission scanning electron microscopy (FE-SEM, Hitachi s-4800 microscope) at 10 kV and transmission electron microscopy (TEM, Tecnai G2 F20 s-Twin microscopy). Raman spectra were measured with WITec Alpha-500 Raman microscope system with a 785 nm laser excitation source. Brunauer-Emmet-Teller (BET) surface area was analysed using Tristar II 3020 for the adsorption of nitrogen.

Electrochemical Characterization

The electrochemical properties were measured in coin cells (CR2430) with lithium foil as the counter electrode. The working electrode consists of the testing material (e.g., Fe_2O_3, Fe_2O_3@C), acetylene black and poly-tetrafluoroethylene (PTFE) (a weight ratio of 80:10:10), which were pasted on Ni foam with 12 mm in diameter. The prepared working electrodes were dried in a vacuum oven at 100 °C over 12 h to remove the solvent. These electrodes had a solid loading of 5.0 mg cm^{-2}. Cells were assembled in a glove box in Ar gas The electrolyte was 1 M $LiPF_6$ in a mixture of dimethyl carbonate, diethyl carbonate and ethylene carbonate (1:1:1 by volume), and the separator was Celgard 2400. The charge/discharge tests were carried out on LAND battery test system (CT 2001A, Wuhan Jinnuo Electronic Co. Ltd. of China) at a constant current density of 200 mA g-1 within a cut-off voltage window of 0.005-3.0 V. Electrochemical impedance spectroscopy (EIS) measurements were conducted on an electrochemical workstation (660D, CHI company, China) with the frequency range from 0.01 Hz to 100 kHz.

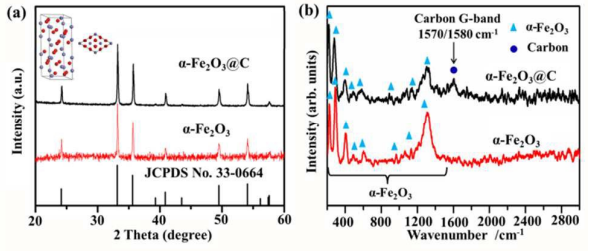

Fig. 2 (a) XRD patterns and (b) Raman spectroscopy of products before (red) and after (black) carbon coating process; inset, the crystal structure of α-Fe_2O_3.

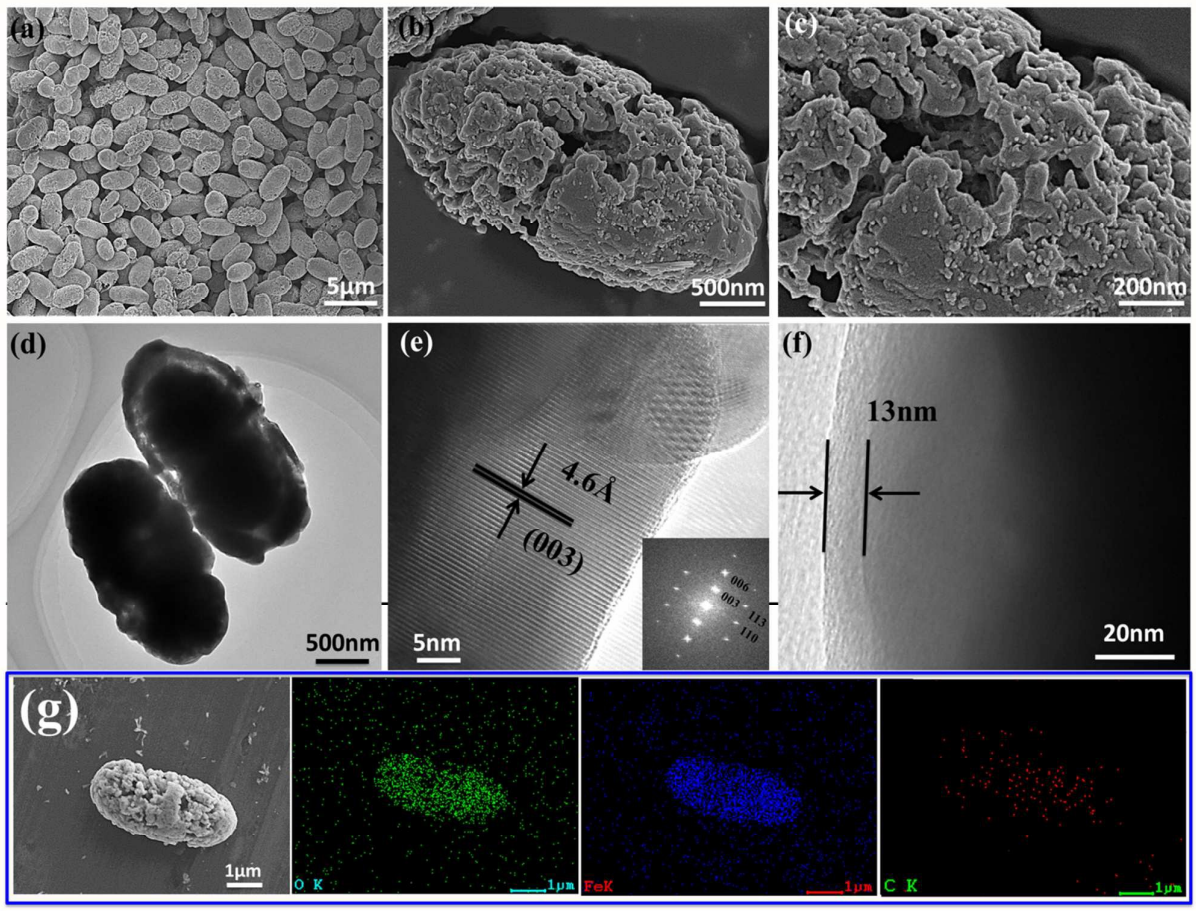

Fig. 3 (a-c) Low and high magnification SEM images (d-f) TEM and high-resolution images with the corresponding fast Fourier transformation pattern (inset) and (g) EDS mappings of α- Fe_2O_3@C microrice.

Results and discussion

The synthetic procedure of porous α-Fe_2O_3-@C microrices is illustrated in Fig. 1. Porous microrices are synthesized in an autoclave first. After separating, the obtained products are mixed with citric acid and then hydrothermally treated. The phase structure analysed from the X-ray diffraction as shown in Fig. 2 is in a good agreement with that of the standard α-Fe_2O_3 (JCPDS card No. 33-0664). In addition, no phase transition takes place during the coating process. The as-synthesized samples have been further characterized by Raman spectroscopy shown in Fig. 2b. It shows that the typical modes for α-Fe_2O_3 are observed in the so-called "finger print" region at low wave numbers for both spectra.[36] Additionally, the G-band at ~1580 cm^{-1}, the featured band in graphite and graphene representing the planar sp2 bonded structure, confirms the carbon coating.[37] The morphology of the as-prepared products was examined using FESEM and TEM. The SEM image of porous α-Fe_2O_3@C microrices in Fig. 3a shows the particles are uniform with rice-like morphology. From the statistics of the particle size distribution (Fig. S1†), the mean length of the microrices is ~3 μm and the diameter ~1.9 μm. The SEM images in Fig. 3b and c show the detailed architecture of the carbon coated α-Fe_2O_3 microrice with highly porous structure indicating an open pore-network within the bulk, which is further confirmed by TEM. Details of the interior structure and carbon-coated surface are revealed by TEM. In the high resolution transmission electron microscopy (HRTEM) image (Fig. 3e) taken along an edge of a Fe_2O_3@C microrice, the lattice fringes with a spacing of 0.46 nm agree with the (003) planes of α-Fe_2O_3 (JCPDS card No.33-0664). In conjunction with fast Fourier transformation (FFT) analysis (Fig. 3e, inset), it is confirmed that the highly crystallized α-Fe_2O_3 is obtained. In Fig.3f, a shell with a thick of 13 nm (highlighted with lines) can be observed. Element mapping in energy dispersive spectroscopy (EDS) shows that Fe, O and C are distributed in the product. Therefore, carbon coated single-crystal α-Fe_2O_3 with a highly porous microstructure has been fabricated successfully.

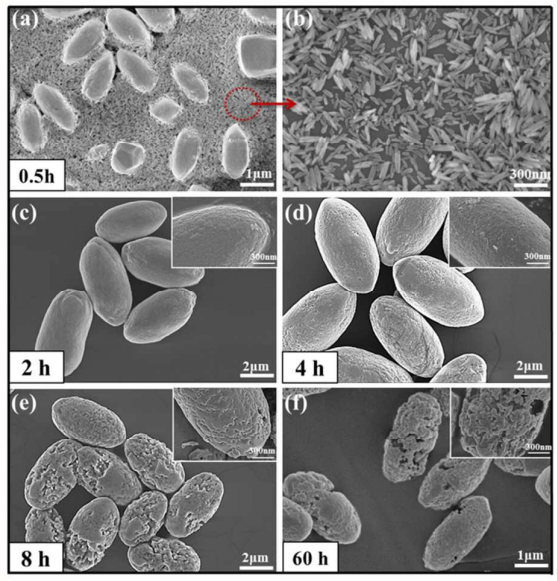

Fig. 4 Low and high magnification SEM images of the α-Fe_2O_3 with a reaction time of 0.5h (a-b), 2h (c), 4h (d), 8h (e) and 60h (f)

In order to elucidate the formation mechanism of porous microrices, the evolution of the samples has been investigated. XRD analysis of all the products (Fig. S2†) shows that the crystal phase of the particles is pure α-Fe_2O_3 and not altered during the formation process. Fig. 4 shows the SEM images of the products with various reaction times (hours). In Fig. 4a, large-scale nanorices and a small amount of microrices can be observed clearly. The morphology of microrice is not uniform. Some of them are ellipsoids with an average length of ~1.5 μm. The high-magnification SEM image of the nanorices is presented in Fig. 4b. The size of the rices ranges widely from tens of nanometers to ~300 nm. It implies that the Ostward ripening process occurs at 0.5 h. When increasing the reaction time to 2 hours, nanorices disappear while microrices still exist as shown in Fig. 3c. The microrices show uniform morphology and size. The length and the diameter of the microrice are ~4μm and ~1.5 μm, respectively. The high magnification SEM image shows that the surface of these micro-particles is nearly smooth. When prolonging the reaction time to 4, micropores appear on the surface of the microrices (Fig. 4d). However, the particles size does not change. When the reaction time is further increased to 8, the rice-like morphology of particle smooth. When prolonging the reaction time to 4, micropores appear on the surface of the microrices (Fig. 4d). However, the particles size does not change. When the reaction time is further increased to 8, the rice-like morphology of particle remains unchanged but the surface becomes noticeably rougher (Fig. 4e). It seems that the pores size and porosity of Fe_2O_3-8 are larger than that of Fe_2O_3-4. Finally, when the reaction time reaches 60, the highly porous Fe_2O_3 microrices are generated (Fig. 4f). The Fe_2O_3-60 particles have the same size rice shape and the largest pores size among all synthetic samples. The results obtained from the time-dependent experiments indicate a chemical etching process which can be used to control the fabrication of porous α-Fe_2O_3 microrices with tunable pore size and pore volume by simple adjusting the etching duration. Nitrogen adsorption–desorption isotherms (Fig. S3†) were employed to measure the pore volume and average pore size of the particles. As shown in Tab.1, the specific area, total pore volume and average pore size of the particles increase monotonously with the etching time.

Tab. 1 Key Parameters of Samples

Product	Reaction Time (hour)	Surface Area ($m^2 g^{-1}$)	Total Pore Volume ($cm^3 g^{-1}$)	Average Pore Size (nm)
Fe_2O_3-2	2	9	0.02	2
Fe_2O_3-4	4	12	0.09	12
Fe_2O_3-8	8	23	0.15	25
Fe_2O_3-60	60	31	0.23	70

The electrochemical performance of the Fe_2O_3-60@C microrice was evaluated as an anode for LIBs. To study the charge-discharge behaviour, Cyclic Voltametry (CV) measurement was conducted. Fig. 5a depicts the representative CVs of the Fe_2O_3-60@C in the potential window of 0.005–3 V at the scan rate of 0.1 mV s^{-1}. In the cathodic polarization process of the first cycle, two obvious peaks were observed at 1.53 and 0.72 V (vs. Li^+/Li), attributed to lithium intercalation in the rice sites and the reduction of Fe^{3+} to Fe^0.[38] Meanwhile, in the anodic polarization process, only one broadened peak was recorded at about 1.6 V (vs. Li^+/Li),

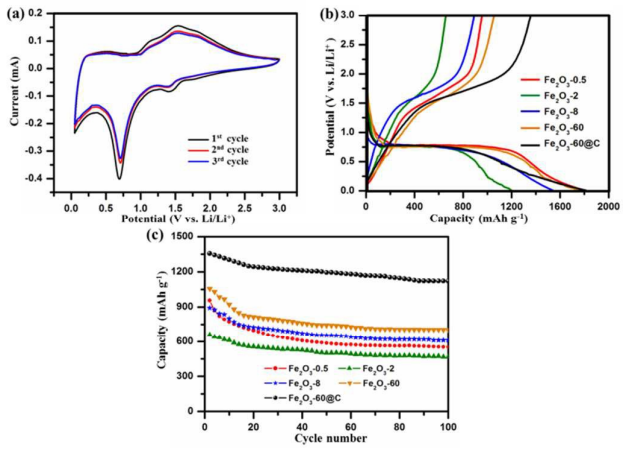

Fig. 5 (a) Cyclic voltammograms of the α-Fe_2O_3-60@C anode at a constant scan rate of 0.1 mV s^{-1}. (b) The first charge/discharge curves of α-Fe_2O_3-0.5, α-Fe_2O_3-2, α-Fe_2O_3-8, α-Fe_2O_3-60 and α-Fe_2O_3-60@C at the current density of 200 mA g^{-1}. (b) Cycling properties of α-Fe_2O_3-0.5, α-Fe_2O_3-2, α-Fe_2O_3-8, α-Fe_2O_3-60 and α-Fe_2O_3-60@C at a current rate of 200 mA g^{-1} between 0.005 to 3 V.

corresponding to the oxidation of Fe^0 to Fe^{3+}.[39] In the 2nd and 3rd cycles, the cathodic peaks shifted to higher potentials with a decrease of the peak intensity and area. While the anodic peak only decrease in peak intensity, revealing that reduction and oxidation proceeds but with some irreversibility.[40] The samples of Fe_2O_3-0.5, Fe_2O_3-2, Fe_2O_3-8, Fe_2O_3-60 and Fe_2O_3-60@C are assembled with lithium into coin cells to investigate the relationship between the electrochemical properties and the pore structures. Fig. 5b shows the first charge/discharge curves of the samples at a current density of 200 mA g^{-1} between 0.005 and 3.0 V. The charge/discharge curves of each electrode have a sloped region between 1.2 and 0.9 V and a long plateau at ~0.75 V, which is in agreement with that of the reported Fe_2O_3 powder. The sloped region is corresponding to the lithium insertion into the crystal structure of Fe_2O_3 the conversion from Fe^{3+} to Fe^{2+}. The long plateau that appeared at ~0.75 V is attributed to the conversion from Fe^{2+} to Fe.[41] The initial discharge capacities were 1812.2, 1204.6, 1543.8, 1752.2 and 2020.8 mA h g^{-1} for the electrodes of Fe_2O_3-0.5, Fe_2O_3-2, Fe_2O_3-8, Fe_2O_3-60 and Fe_2O_3-60@C,respectively, with the corresponding first cycle charge capacities of 956.8, 659, 892, 1056 and 1507.9 mAh g^{-1}. Accordingly, the coulombic efficiencies of the electrodes can be achieved as 52.8%, 54.7%, 57.8%, 60.3% and 74.6% for Fe_2O_3-0.5, Fe_2O_3-2, Fe_2O_3-8, Fe_2O_3-60 and Fe_2O_3-60@C, respectively. The irreversible capacity of the electrodes during the initial cycle may be attributed to the formation of solid/electrolyte interface (SEI) layer and the decomposition of electrolyte.[42] Obviously, the initial charge/discharge capacity and the coulombic efficiency of Fe_2O_3-60@C electrode is much higher than those of other three electrodes. The highly porous structure of Fe_2O_3-60@C significantly enhances the effective electrode-electrolyte contact areas and the amount of electro-active sites. Meantime, the carbon layer partly protects from the formation of SEI layer. Because of the a synergetic contribution from the porous structure and the carbon layer, both the initial charge/discharge capacity and the coulombic efficiency of Fe_2O_3 are increased.[15,16]

Fig. 5c shows the charge/discharge cycling performance for Fe_2O_3-0.5, Fe_2O_3-2, Fe_2O_3-8, Fe_2O_3-60 and Fe_2O_3-60@C at the current density of 200 mAg^{-1}. After 100 cycles, the Fe_2O_3-60@C electrode remain the reversible capacity of 1107 mAh g^{-1}, up to 83% of its initial capacity, 552, 467, 610 and 704 $mAhg^{-1}$ for the electrodes of Fe_2O_3-0.5, Fe_2O_3-2, Fe_2O_3-8 and Fe_2O_3-60, respectively. Compared to other three microrice electrodes, there was a rapid capacity decrease during the first 40 cycles for Fe_2O_3-0.5 electrode. Because it mainly contains Fe_2O_3 nanoparticles, the poor capacity retention is probably caused by the particle aggregation and electrode pulverization.[42-45] The cycling stability of Fe_2O_3-0.5 electrode is inferior to that of the other four electrodes with microrices, indicating the single-crystal microrice has a better structural stability than nano-particles. Additionally, Fe_2O_3-2 has a lower capacity but better cyclability than that of Fe_2O_3-8 and Fe_2O_3-60. This indicates that the increase of the pore-size and porosity of the microrice leads to an increase of capacity with a drop of the capacity retention which is attributed to the increase of active sites for

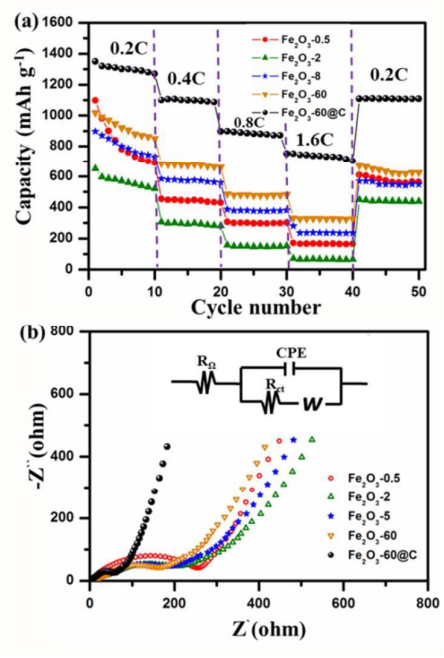

Fig. 6 (a) rate capacity retention at varied C-rates and (b) Nyquist plots of α-Fe2O3-0.5, α-Fe2O3-2, α-Fe2O3-8, α-Fe2O3-60 and α-Fe2O3-60@C.

lithium storage and structure instability. Fe_2O_3-60@C electrode possesses a much higher capacity and better cycling stability than that of Fe_2O_3-60 electrodes and other three electrodes, demonstrating coating carbon on the surface of porous microrices can accommodate the volume change of the Li^+ insertion–extraction during charge–discharge processes. (Fig. S4† shows the SEM images of active materials after 100 cycles.)

Fig. 6a shows the capacity retentions at varied C-rates from 0.2 to 1.6 C (200, 400, 800 and 1600 mA g^{-1}). The batteries were cycled 10 times at each C-rate. Among the uncoated microrices, Fe_2O_3-60 has the largest capacity retention and Fe_2O_3-8 and Fe_2O_3-2 follows. The trend is in the same order of the pore size and porosity. The reversible capacities of the Fe_2O_3-60@C electrode are about 1270, 1087, 871, and 702.7mAh g^{-1} at the current densities of 0.2 C, 0.4 C, 0.8 C and 1.6 C, respectively. Their specific capacities are much higher than those of the as-synthesized Fe_2O_3 electrodes without carbon coating. It indicates that the improvement in electrochemical properties should not only attribute to structural optimization of the iron oxide, but also the thin carbon layer outside the particles. Fig. 6b shows the electrochemical impedance spectroscopy (EIS) spectra of these four electrodes collected from fresh cells. The electrochemical system is simply modeled by a Randles equivalent circuit as shown in the inset where R_Ω is the ohmic resistance, CPE is the double-layer capacitance, R_{ct} is the charge transfer resistance, and W is the Warburg impedance describing the solid-state diffusion of Li^+ in α-Fe_2O_3.[46] The diameter of the semicircle in the high–medium-frequency region for Fe_2O_3-0.5, Fe_2O_3-2, Fe_2O_3-8, Fe_2O_3-60 and Fe_2O_3-60@C electrodes are 249Ω, 190Ω, 175Ω, 149Ω and 52Ω, respectively, with the same size of the

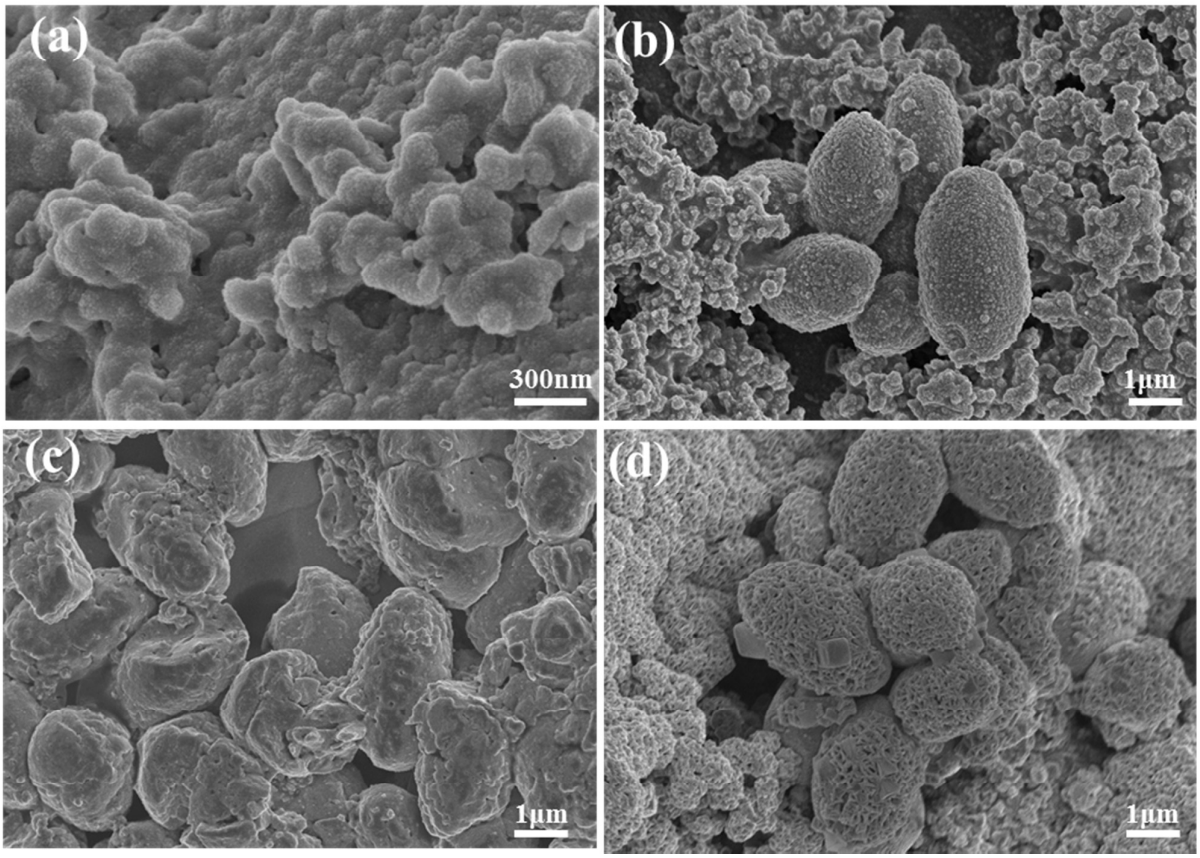

Fig.7 The SEM images of Fe_2O_3-0.5, Fe_2O_3-8, Fe_2O_3-60 and Fe_2O_3-60@C after 50 cycles.

electrodes. The impedance of porous microrice electrode with carbon coated is much smaller than that of pristine Fe_2O_3 nano/micro particle electrodes, indicating the improved conductivity of the porous α-Fe_2O_3 microrices after carbon coating.

In order to further understand the effect of the porous structure and the coated carbon on the electrochemical performance of Fe_2O_3 particles, the morphology of the four electrodes, Fe_2O_3-0.5, Fe_2O_3-8, Fe_2O_3-60 and Fe_2O_3-60@C after 50 cycles are measured by SEM, and displayed in Fig. 7 a-d, respectively. As shown in Fig. 7a, the nanorices aggregated and the morphology of the materials was destroyed, indicating a poor structural stability of Fe_2O_3-0.5 nanorices. Different from the morphology shown in Fig. 7a, it can be observed in Fig. 7b that the Fe_2O_3-8 microrices are well dispersed on the electrodes without obvious aggregation, which demonstrates the better stability than the as-fabricated nanorice electrode. In the Fig.7c, the Fe_2O_3-60 micro-particle are still well-separated as Fe_2O_3-8. However, a part of the particles do not present rice-like morphology any longer. This mainly because the highly porous structure of the microrices is destroyed during the cycling process. Compared with Fe_2O_3-60, Fe_2O_3-60@C porous microparticles keep their rice-like morphology and porosity. Meanwhile, aggregation does not take place during the cycling. The results reveal (1) the microrices present better stability; (2) the increased porosity leads to the poor structure stability; (3) carbon layer can greatly protect the porous microrices from being destroyed in the charge-discharge process.

On the basis of above analysis, it is found that the increase of the average pore-size and the total porosity will lead to an increase of the capacity and a decrease of the cycling stability

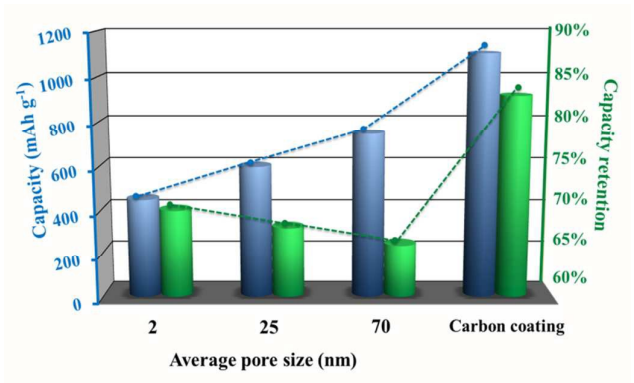

Fig.8 The capacities and capacity retention with different porosity of α-Fe_2O_3 particles for the hundredth circle.

in micro-sized porous Fe_2O_3 system as shown in Fig. 8. A plausible mechanism may be that the increase in the pore size and volume provides extra surface area, resulting in a high capacity, however, the side effect is that the increased defects reduces the stability and shortens the lifetime of the electrode. Coating carbon layer on the surface of materials not only stabilize the porous structures and but also improve the conductivity greatly so as to the enhanced LIB performance.

Conclusions

In summary, we have successfully synthesized porous single-crystal α-Fe_2O_3 microrices by a facile hydrothermal process. The size and porosity of the microrices can be adjusted in a wide range by controlling the reaction parameters. Electrochemical characterizations reveal that the increase of both the pore size and porosity of the porous microrices induced by the etching process significantly improves the capacity but lower the cyclability. This is mainly because the pores enlarges the specific area and increases the structural defects either. However, carbon coating on the surface of electrode materials with highly porous structure can greatly protect the structure from being destroyed during cycling, resulting in better cyclability. At the same time, the carbon layer also improves the conductivity of the α-Fe_2O_3 microrices greatly. Due to the synergistic effect of the highly porosity and carbon layer, α-Fe_2O_3@C porous microrices exhibit much enhanced LIB performance. The structural optimization strategy in this work can be developed into a general procedure to fabricate other micro-scale porous oxide frameworks, which provides a great promise to the development of micro-scale LIB materials.

Acknowledgements

This work was financially supported by the National Natural Science Foundation of China (Grant No. 21376192, 20851001 and 61275105), International Cooperative Program (Grant No. 201410780). Partial support is provided by the Nanjing University Creation Talent Program (Grant No.021314310023).

Notes and references

1 P. Poizot, S. Laruelle, S. Grugeon, L. Dupont and J. M. Tarascon, *Nature*, 2000, **407**, 496-499.
2 Y. Wang and G. Cao, *Adv. Mater.*, 2008, **20**, 2251-2269.
3 H. Wu, G. Chan, J. W. Choi, Y. Yao, M. T. McDowell, S. W. Lee, A. Jackson, Y, Yang, L. Hu and Y. Cui, *Nature nanotech.*, 2012, **7**, 310-315.
4 T. Ohsaki, M. Kanda, Y. Aoki, H. Shiroki and S. Suzuki, *J. Power Sources*, 1997, **68**, 102-105.
5 F. Leroux, K. Metenier, S. Gautier, E. Frackowiak, S. Bonnamy and F. Beguin, *J. Power Sources*, 1999, **81**, 317-322.
6 B. Jang, O. B. Chae, S. K. Park, J. Ha, S. M. Oh, H. B. Na and Y. Piao, *J. Mater. Chem. A*, 2013, 1, 15442-15446.
7 B. J. Landi, M. J. Ganter, C. D. Cress, R. A. DiLeo and R. P. Raffaelle, *Energy Environ. Sci.*, 2009, **2**, 638-654.
8 P. Simon, Y. Gogotsi and B. Dunn, *Science*, 2014, **343**, 1210-1211.
9 D. Ma, Z. Cao, H. Wang, X. Huang, L. Wang and X. Zhang, *Energy Environ. Sci.*, 2012, **5**, 8538-8542.
10 T. H. Kim, J. S. Park, S. K. Chang, S. Choi, J. H. Ryu and H. K. Song, *Adv. Energy Mater.*, 2012, **2**, 860-872.
11 J. Jiang, Y. Li, J. Liu and X. Huang, *Nanoscale*, 2011, **3**, 45–58.
12 J. S. Kim, K. Kim, W. Cho, W. H. Shin, R. Kanno and J. W. Choi, *Nano Lett.*, 2012, **12**, 6358-6365.
13 J. Ye, A. C. Baumgaertel, Y. M. Wang, J. Biener, and M. M. Biener, *ACS Nano*, 2014, doi: 10.1021/nn505490u
14 H. Zhang, X. Yu, P V. Braun, *Nature Nanotechnology*, 2011, **6**, 277-281.
15 J. Wang, Q. Zhang, X. Li, B. Zhang, L. Mai and K. Zhang, *Nano Energy,* 2015, **12**, 437-446.
16 Q. Zhang, J. Wang, D. Xu, Z. Wang, Xi. Li and K. Zhang, *J. Mater. Chem. A,* 2014, **2**, 3865-3874.
17 W. Xiao, Z. Wang, H. Guo, X. Li, J. Wang, S. Huang and L. Gan, *Appl. Surf. Sci.,* 2013, **266**, 148-154.
18 W. Xiao, Z. Wang, H. Guo, Y. Zhang, Q. Zhang and L. Gan, *J. Alloys Comp.,* 2013, **560**, 208-214.
19 M. V. Reddy, T. Yu, C. H. Sow, Z. X. Shen, C. T. Lim, G. V. S. Rao and B. V. R. Chowdari, *Adv. Funct. Mater.*, 2007, **17**, 2792.
20 J. Chen, L. Xu, W. Li and X. Gou, *Adv. Mater.*, 2005, **17**, 582-586.
21 S. Chaudharia and M. Srinivasan, *J. Mater. Chem.*, 2012, **22**, 23049- 23056.
22 B. Wang, J. S. Chen, H. B. Wu, Z. Wang and X. W. Lou, *J. Am. Chem. Soc.*, 2011, **133**, 17146-17148.
23 J. Zhu, Z. Yin, D. Yang, T. Sun, H. Yu, H. E. Hoster, H. H. Hng, H. Zhang and Q. Yan, *Energy Environ. Sci.*, 2013, **6**, 987–993.
24 P. Tartaj, M. P. Morales, T. G. Carreno, S. V. Verdaguer and C. J. Serna, *Adv. Mater*., 2011, **23**, 5243-5249.
25 M. Park, X. C. Zhang, M. D. Chung, G. B. Less and A. M. Sastry, *J. Power Sources*, 2010, **195**, 7904-7929.
26 J. Jiang, Y. Li, J. Liu, X. Huang, C. Yuan and X. W. Lou, *Adv. Mater.*, 2012, **24**, 5166–5180.
27 X. J. Zhu, Y. W. Zhu, S. Murali, M. D. Stoller and R. S. Ruoff, *ACS Nano*, 2011, **5**, 3333-3338.
28 W. Liu, P. Gao, Y. Mi, J. Chen, H. Zhou and X. Zhang, *J. Mater. Chem. A*, 2013, **1**, 2411-2417.
29 X. Li, Y. Ma, L. Qin, Z. Zhang, Z. Zhang, Y. Zheng and Y. Qu, *J. Mater. Chem. A*, 2015, **3**, 2158-2165.
30 Q. An, P. Zhang, Q. Wei, L. He, F. Xiong, J. Sheng, Q. Wang and L. Mai, *J. Mater. Chem. A*, 2014, **2**, 3297-3302.
31 K. A. Kwon, H. S. Lim, Y. K. Sun and K. D. Suh, *J. Phys. Chem. C*, 2014, **118**, 2897-2907.
32 Y. Ren, A. R. Armstrong, F. Jiao and P. G. Bruce, *J. Am. Chem. Soc.*, 2009, **132**, 996-1004.
33 J. Chen, T. Zhu, X. Yang, H. Yang and X. W. Lou, *J. Am. Chem. Soc.*, 2010, **132**, 13162-13164.
34 H. Liu, G. Wang, J. Wang and David Wexler, *Electrochemistry Communications*, 2008, **10**, 1879-1882.
35 J. S. Chen, Y. Zhang and X. W. Lou, *ACS Appl. Mater. Interfaces,* 2011, **3**, 3276-3279.
36 D. L. A. deFaria, S. V. Silva and M. T. deOliveira, *J. Raman Spectrosc.*, 1997, **28**, 873-878.
37 A. Brandt and A. Balducci, J. Power Sources, 2013, **230**, 44-49.
38 R. Ma, L. He, Z. Lu, S. Yang, L. Xia and J. C. Y. Chung, *Cryst. Eng. Comm.*, 2012, **14**, 7882-7887.
39 J. Zhu, T. Zhu, X. Zhou, Y. Zhang, X. W. Lou, X. Chen, H. Zhang, Huey H. Hnga and Q. Yan, *Nanoscale*, 2011, **3**, 1084-1089.
40 D. Zhang, Y. Li, M.i Yan and Y. Jiang, *Chem. Electro. Chem.*, 2014, **1**, 1155-1160.
41 G. Wang, H. Wang, S. Cai, J. Bai, Z. Ren and J. Bai, *J. Power Sources*, 2013, **239**, 37-44.
42 Z. Wang, D. Luan, S. Madhavi, Y. Hud and X. W. Lou, *Energy Environ. Sci.*, 2012, **5**, 5252-5256.

43 D. Zhang, Y. J. Mai, J. Y. Xiang, X. H. Xia, Y. Q. Qiao and J. P. Tu, *J. Power Sources*, 2012, **217**, 229-235.
44 H. Li, L.H. Shi, Q. Wang, L.Q. Chen and X. J. Huang, *Solid State Ionics*, 2002, **148**, 247-258.
45 Y.G. Guo, J.S. Hu and L. J. Wan, *Adv. Mater.*, 2008, **20**, 2878-2887.
46 Y. M. Lin, P. R. Abel, A. Heller and C. B. Mullins, *J. Phys. Chem. Lett.*, 2011, **2**, 2885-2891.

Graphical abstract for contents entry

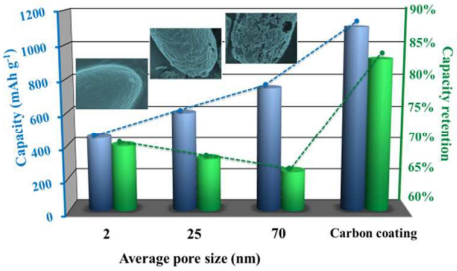

Porous α-Fe_2O_3 microrices have been prepared as a model system to study structural optimization of porous microstructure on LIB performance.